Journal of Alloys and Compounds 947 (2023) 169614

Contents lists available at ScienceDirect

Journal of Alloys and Compounds

journal homepage: www.elsevier.com/locate/jalcom

The effect of multiple thermal cycles on Ti-6Al-4V deposits fabricated by wire-arc directed energy deposition: Microstructure evolution, mechanical properties, and corrosion resistance

Zidong Lin [a,b,c], Constantinos Goulas [c], Yan Li [b], Yongzhe Fa [a,b], Lixue Qiao [d], Zhen Sun [a,b], Rui Cao [d], Wei Ya [e], Xinghua Yu [a,b,*]

[a] School of Materials Science & Engineering, Beijing Institute of Technology, Beijing 100081, China
[b] Beijing Institute of Technology Chongqing Innovation Center, Chongqing 401120, China
[c] University of Twente, Faculty of Engineering Technology, Department of Design Production & Management, P.O. Box 217, 7500 AE, Enschede, the Netherlands
[d] School of Materials Science and Engineering, Lanzhou University of Technology, Lanzhou 730050, China
[e] Rotterdam Additive Manufacture Fieldlab (RAMLAB), Scheepsbouwweg 8 F6, 3089JW Rotterdam, the Netherlands

ARTICLE INFO

Article history:
Received 4 December 2022
Received in revised form 7 March 2023
Accepted 8 March 2023
Available online 11 March 2023

Keywords:
Wire-arc directed energy deposition (Wire-arc DED)
Ti-6Al-4V alloy
Thermal cycle
Microstructure evolution
Microhardness
Corrosion resistance

ABSTRACT

Thermal cycles have an important effect on the microstructure and properties of the components fabricated by wire-arc directed energy deposition (wire-arc DED). In this study, a Gleeble thermal-mechanical simulator was adopted to create closer-to-reality thermal cycles with the assistance of a numerical simulation model and experimental Ti-6Al-4V deposition. Step-by-step microstructure evolution, including α_m, retained β, and GB α, microhardness gradual variation, and the corrosion resistance change before and after the entire thermal cycle were investigated. Therefore, combining phase orientation and high-magnification morphology, transformed and untransformed α that occurred in low- and medium-temperature thermal cycles can be distinguished. After the entire thermal cycle, α_m laths coarsened from ~1 μm to ~1.2 μm, and the content of retained β phase became more and more. The α_m formed around grain boundaries partially disappeared and was occupied by α laths from the inner grain. GB α was more continuously distributed along prior β grain boundaries due to its lower formation temperature during the subsequent thermal cycles that were occurring incomplete α→β transformation. The severe preferential orientation of α phases formed after the deposition and high-temperature thermal cycle was also alleviated through the twice low-temperature thermal cycles. Besides, the microhardness decreased from 318.78 ± 7.5 HV to 285.17 ± 5.3 HV after the high-temperature thermal cycle but eventually increased significantly to 330.5 ± 6.4 HV after experiencing the final low-temperature thermal cycle. The corrosion resistance decreased after the entire thermal cycle, indicating a performance difference between the top and bottom regions of the Ti-6Al-4 V component fabricated by wire-arc DED.

1. Introduction

Wire-arc directed energy deposition (Wire-arc DED) has been regarded as a practical and cost-effective processing method for academic research and engineering applications [1–3]. It has distinctive advantages, including high deposition rate and materials utilization, short production cycle, and lead time, as well as being competent for fabricating large-scale metallic components with strongly complex shapes [4]. Until today, many alloy systems have been successfully adopted in wire-arc DED processes on demand, mainly including steels, aluminum alloys, nickel alloys, titanium alloys, and various kinds of functionally gradient alloys such as Al-Cu, Fe-Ni, Ni-Ti, and Fe-Al, etc. Ti-6Al-4 V is the most widely used α + β type titanium alloy among the aforementioned structural alloys. Its superior comprehensive properties include low density, lightweight, high fracture toughness, high heat resistance, high specific strength ratio, high fatigue strength, high crack growth resistance, and corrosion resistance [5–7]. Particularly, Ti-6Al-4 V has a stable microstructure, high creep resistance up to 500 °C, and good resistance to seawater and heat-resistant salt stress corrosion. Such superior characteristics greatly support its application to fabricating

* Corresponding author at: School of Materials Science & Engineering, Beijing Institute of Technology, Beijing 100081, China.
E-mail address: xyu@bit.edu.cn (X. Yu).

https://doi.org/10.1016/j.jallcom.2023.169614
0925-8388/

long-term serving components in medium-temperature environments, for instance, rocket engine shells, aero-engine compressor discs and blades, and more.

Many studies have focused on fabricating Ti-6Al-4 V components using the wire-arc DED process. However, a common problem was observed: multiple thermal cycles experienced during deposition always cause unfavorable microstructure formation and distribution, further leading to deterioration and anisotropy. For example, Zhou et al. [8] found that thin walls would experience more thermals above β transus temperature than thick walls, resulting in solid solution hardening due to more alloying elements dissolved into β phases. This means that the deposited metal will be affected by the residence time and the cooling rate above the β transus temperature when it undergoes subsequent thermal cycles, which further play a role in the final microstructure so it needs to be considered in the current study. Moreover, the temperature and number of subsequent thermal cycles experienced by the deposited metal have an impact on the uniformity (segregation) of the final element distribution, which in turn affects the microstructure such as residue stabilized β content and mechanical properties of the component. For example, G. Xian et al. [9] mentioned that the regions with more thermal cycles below the β transus temperature were more likely filled with α′ martensite and fine-secondary α with a tangled dislocation, which was caused by more significant amounts of nitrogen accumulation. Therefore, this region exhibited a larger tensile strength and microhardness, followed by severe mechanical anisotropy within the final deposited component. Therefore, it is necessary and meaningful to observe the changing of β content concerning thermal cycles. J.R. Kennedy et al. [10] investigated the microstructure transition gradients of Ti-5Al-5 V-5Mo-3Cr/Ti-6Al-4 V alloys and observed the orientation of α laths near and far away from the interface. Distinctive thermal cycles change the state of prior β grains, such as size, solid solution elements, dislocation density surrounding the interface, etc. As a result, only 2/12 of preferred BOR orientations [11] of α laths were selected at the interface. In contrast, the α variants became more randomly distributed when the distance was far from the interface. Under the premise of this finding, it is reasonable to speculate that the orientation of the α phases during the deposition of a single-bead wall of Ti-6Al-4 V will also be indirectly changed by the influence of subsequent thermal cycles on its parent phase β. So, the step-by-step characterization of the distribution of α-phase orientation changes with thermal cycles is helpful to establish the relationship between different orientations and properties. In addition, as mentioned earlier, the excellent corrosion resistance of titanium alloys increases its application range and cases. However, there have been relatively few and unclear reports on the corrosion resistance of Ti-6Al-4 V alloy manufactured by additive manufacturing processes so far. Except for the microstructure evolution and the corresponding influence on mechanical properties, various thermal cycles would also contribute to a change in the corrosion resistance of Ti-6Al-4 V deposits—for example, L.Y. Chen et al. [12] found that the corrosion resistance along the cross-sectional plane (X-) perpendicular to the laser moving direction was ~20 % lower than the Y- and Z- planes. More artifact holes are induced in the X-plane due to ununiform laser intensity distribution between two neighboring printing lines. However, the zigzag scanning strategy brought more heating (thermal cycles) in the Y- and Z-planes, so the microstructure exhibited more dense morphology, significantly improving the electrochemical resistance. Besides, B. Wu et al. [13] also tested the corrosion resistance at different locations of the deposited Ti-6Al-4 V sample. The anisotropic corrosion behavior was proved owing to the anisotropy in microstructure, phase structure, grain size, and orientation. The difference originated from the different thermal histories to a certain degree, although on the scope of a microscopic scale.

It is undeniable that there have been many studies on the effect of multiple thermal cycles on the microstructure and properties of various additive-manufactured alloys. The previous studies typically investigated different positions of the sample, such as the top, middle, and bottom sections, to represent the result of different thermal cycles. The drawback of such studies is that the characterization will be affected by the initial locations and states of microstructure at different positions. Therefore, not only can the phase evolution not be reflected, but the comparison of the end-state microstructure needs to be more intuitive. Moreover, the experienced thermal cycle frequencies are unclear and hard to determine, meaning that they would be easily affected by the extracted sample position. Therefore, one aim of this study is to focus on revealing the microstructure evolution mechanism at the exact location during multiple thermal cycling of wire-arc DED process by step-by-step characterization. Besides, even though a majority of studies have summarized the effect of microstructure changes on corrosion resistance, this is only valid when the phases which contribute to properties change to a certain degree. In this study, although the microstructure difference between the adjacent deposition layers is visible on a micro-scale, it is not apparent or indistinguishable from the different views of inter-layer corrosion resistance. Therefore, the authors consider it more intuitive and accurate to study the accumulation of corrosion performance changes before and after the entire thermal cycle. The corrosion resistance was only characterized before (AD state) and after the entire thermal cycle to reflect the greatest anisotropy of the deposited component (commonly refers to the final layer and the middle stable region according to different thermal histories).

Moreover, for the applied components, the weakest location always needs to be concerned and prevented, generally referring to the last deposited several layers in AM components. Since the microhardness of the sample surface is indented with multiple points with a small load, local microstructure changes can be reflected in the microhardness. Unlike corrosion resistance, step-by-step characterization of microhardness is meaningful and adopted in this study. Consequently, a numerical simulation was first used to create a series of thermal cycle curves appointed as references for consequent experiments. A Gleeble thermal-mechanical simulator was applied to simulate the thermal cycles on the same as-deposited (AD) sample according to the simulated values, mainly referring to heating rate (HR), peak temperature (PT), and cooling rate (CR). The microstructure and microhardness of the same targeted region in the sample were studied after each thermal cycle. At last, the electrochemistry corrosion resistance of the sample was investigated before and after the entire thermal cycle.

2. Numerical simulation & experiments

2.1. Simulation of theoretical thermal cycle curve (TTCC)

In this study, reasonable theoretical thermal cycle curves were obtained by the model built in a previously published paper [14] to reference subsequent experiments. ABAQUS was used as a simulation tool, and the effective simulation heat input was set up to be 1.52 kJ/mm.

2.2. Deposition of Ti-6Al-4V wall

In this study, a wrought Ti-6Al-4 V base plate of 380 × 100 × 30 mm^3 was used. Commercially available Ti-6Al-4 V solid wires (3Dprint AM TI-5, Voestalpine Böhler Welding) with a diameter of 1.2 mm were employed as the feedstock. The chemical composition of wrought Ti-6Al-4 V base plate and used Ti-6Al-4 V wire were listed in Table 1. The entire deposition process was conducted in a closed chamber flashed with shielding gas supplied by

Table 1
Chemical composition of the used materials.

Materials	Al	V	Fe	C	Ti
Ti-6Al-4 V wire used	5.5–6.76 %	3.5–4.5 %	< 0.25 %	< 0.08 %	Bal.
Wrought Ti-6Al-4 V base	6.28	4.15	0.15	0.03	Bal.

Table 2
Deposition parameters.

Variables	Parameters
Current	220 [A]
Voltage	16.1 [V]
Deposition speed	420 [mm/min]
Step up distance	4.5 [mm]
Shielding gas flow rate (30 % He, 70 % Ar)	22 [L/min]
Protective gas flow rate (99.999 % Ar)	150 [L/min]
Interlayer temperature	25 [°C]
Contact tip-to-work distance (CTWD)	1 [mm]
Wire stick-out distance	15 [mm]
Deposition strategy	Oscillation reciprocating path
Polarity	Direct current, reversed polarity (wire: positive, base: negative)
Molten droplet transfer mode	Super Active Wire Process (modification of short-circuit)

Air Products. Shielding gas with the composition mixture of argon and helium was provided through the GMAW torch nozzle. A cylindrical tracing shielding device filled with 99.999 % pure argon gas was fixed on the GMAW torch to protect the melt as it cools. The deposition was carried out using a Panasonic robotic arm and a power source integrated by Valk Welding. The software used for designing the deposition tool path was Autodesk PowerMill (Autodesk B.V, Hoofddorp, The Netherlands). Process parameters and other conditions were stored using the RAMLAB MaxQ system. The torch was continuously positioned perpendicular to the workpiece (PA position). An oscillation strategy was adopted to obtain wide beads [15] and the deposition parameters used are summarized in Table 2. After deposition of each layer, the wall was cooled within the inert environment until the out surface was measured to be at ambient temperature ~25 °C, and the contact tip-to-work distance (CTWD) was kept to be around 1 mm higher during the whole deposition process. Layer-by-layer reciprocating deposition strategy was applied to ensure the uniform height of the wall. The experimental conditions, such as heat input which is the most important, are kept the same as the ones applied in the simulation process. The cross-section of the deposited wall and the investigated sample position are shown in Fig. 1.

Extracting a sample far from the base is preferable to eliminate the influence of base materials composition on the thermal cycle mechanism. Therefore, depositing a single-bead wall with multiple layers and getting a sample from the final deposited layer (no experienced thermal cycles) was adopted as an effective method to improve the result accuracy of the microstructural evaluation.

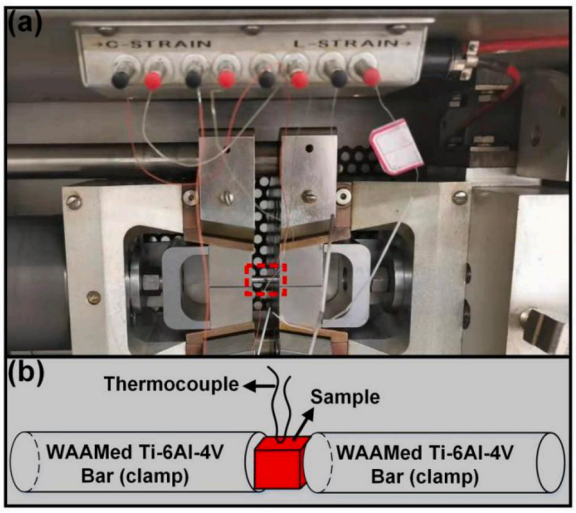

Fig. 2. Setup of TMS test: (a) physical map, (b) zoomed-in picture of the marked section in (a).

2.3. Gleeble thermal-mechanical simulation (TMS) test

Based on the output theoretical thermal cycle curve and actual deposition conditions, a Gleeble TMS test (Gleeble 3500-GTC with the integration of high-temperature K type Thermocouple - 1300 °C) was carried out to produce real thermal cycles on the investigated sample. The clamps on both sides of the sample were obtained from the deposited wall to get a closer thermal conductivity with the deposition (thermal cycle) process. The sample was placed in the isothermal zone, and the temperature difference along the directions perpendicular to the sample was ignored. The temperature distribution of the entire sample was considered uniform and equal to the set value of the central temperature-controlled thermocouple. The observation surface of the sample was marked and kept in the same orientation (forward) during each heating of the thermal cycle. The setup of the TMS test can be seen in Fig. 2.

2.4. Characterization methods

The sample (5 × 5 × 5 mm^3) used for microstructural characterization was taken from the final deposited layer of the wall and etched by a mixture solution of $HF+HNO_3+H_2O$ = 1:6:47 for optical microscopy (Keyence VHX-5000, Osaka, Japan). High-resolution microstructural features were observed using a JEOL FEG-SEM JSM 5600 F scanning electron microscope (SEM) with an electron backscattered diffraction detector (EBSD, Bruker). It is pointed out that the same area of the same sample was observed multiple times by OM, SEM, and EBSD techniques to more clearly reveal the phase evolution. Therefore, the position of the trigeminal grain boundaries with unique shapes and easy identification was first selected as the

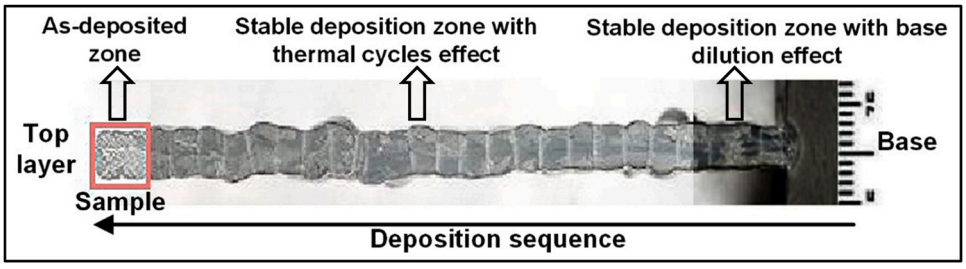

Fig. 1. Cross-section and investigated sample position of the Ti-6Al-4 V single-bead wall.

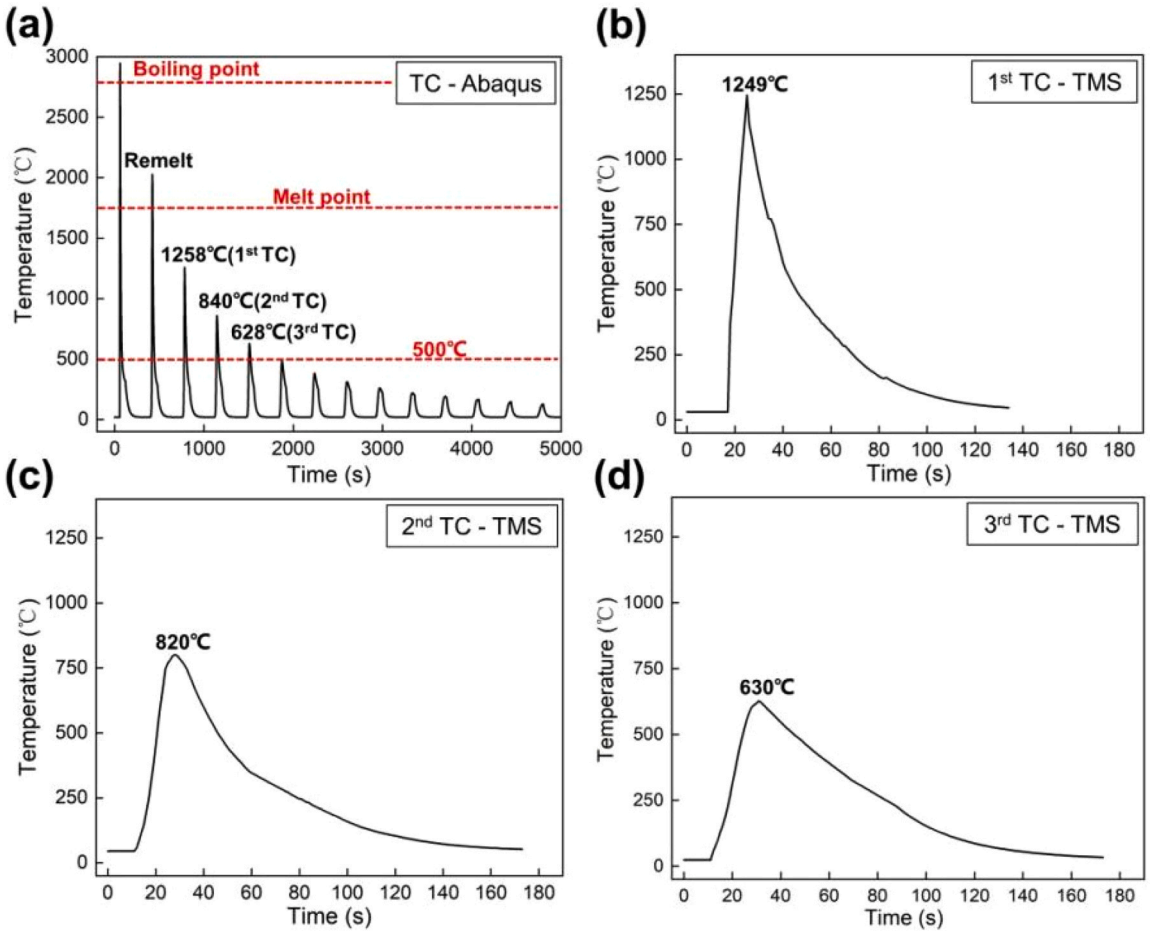

Fig. 3. Thermal Cycle Curves: (a) TTCC, (b) RTCC-1st thermal cycle, (c) RTCC-2nd thermal cycle, (d) RTCC-3rd thermal cycle.

observation area. Then the distance between this observation area and the four edges of the sample was calibrated. Vickers microhardness ($HV_{0.25}$, with 0.025 kgf) was measured on the cross-section of the sample using a Struers DuraScan-70 machine (Struers Inc., Cleveland, OH, USA). Multiple points were measured each time to take an average value. Electrochemical measurements in this study mainly contain Electrochemical impedance spectra (EIS) plus Tafel and potentiodynamic polarizations, which were performed in 3.5 wt % NaCl solutions at 25 ± 1 ℃ using a PARSTAT 4000 electrochemical workstation with a three-electrode cell. The 3.5 wt % NaCl solution is the typical electrolyte used for titanium alloy manufactured by wire-arc DED process. All the potential measurements were carried out regarding the saturated calomel electrode (SCE). A platinum sheet of dimensions 1.5 cm × 1.5 cm was employed as the counter electrode. Before EIS, Tafel, and potentiodynamic polarization tests, the samples were kept in the solution for sufficient time to attain a stable OCP. EIS was performed in the frequency range of 0.01 Hz - 100 kHz with an amplitude of 10 mV. The Tafel polarization measurements were performed in the potential range of − 1 V to + 2 V at a scan rate of 5 mV/s in 3.5 wt % NaCl solution. Since all microstructure characterization and hardness tests were performed on the same sample, each test consumed a certain thickness of the sample, especially each EBSD and corrosion resistance test consumed too much sample thickness, as well as the total thickness of the sample (layer height) was small. Therefore, apart from considering the accumulation of corrosion performance changes to be easily observed, aiming to ensure that the samples were sufficient to meet as many tests as possible, the corrosion resistance tests of 1st TC and 2nd TC were not carried out. Each electrochemistry corrosion test was performed three times on the same surface of the sample to confirm its reproducibility.

3. Results & discussion

3.1. Thermal cycle curve (TCC)

The Theoretical Thermal Cycle Curve (TTCC) output from ABAQUS and Real Thermal Cycle Curve (RTCC) formed from thermal-mechanical simulation (TMS) are shown in Fig. 3. Under this experimental condition, the as-deposited (AD) material first undergoes remelting. However, the solid-liquid transition during the remelting process does not belong to the category of thermal cycling, so it is not considered at this moment. Also, the remelted material can still be regarded as an AD state and experience the consequent thermal cycles. As mentioned above, the Ti-6Al-4 V alloy can serve up to 500 ℃, which means that the microstructure is relatively stable and hard to transform below 500 ℃. Therefore, in this study, the thermal cycles above 500 ℃ play a significant role in the microstructure evolution. Three typical temperatures, including 1258 ℃ (1st TC), 840 ℃ (2nd TC), and 628 ℃ (3rd TC), respectively, located in the entire β region, α + β high-temperature region, and α + β low-temperature region were determined for thermal cycle experiment as shown in Fig. 3(a). Besides, Fig. 3(b)-(d) shows the thermal cycles of the sample. The Gleeble TMS performs the real heating and cooling process according to the simulation results (Fig. 3(a)). In general, it can be found that the output results of peak temperature, heating, and cooling rate are highly similar to the simulation results since the minor error range of peak temperature is within ± 20 ℃. Apart from that, the cooling rate

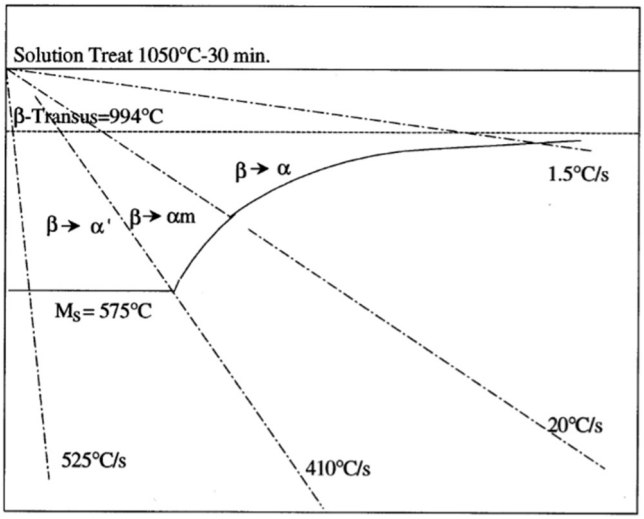

Fig. 4. α formation under different cooling rates [17].

decreases as the sample temperature drops down, and the average cooling rate above 500 ℃of the whole thermal cycle also becomes slower and slower (AD: 63.2 ℃/s, 1st TC: 33.2 ℃/s, 2nd TC: 18.3 ℃/s, 3rd TC: 9.5 ℃/s) as the progress of thermal deposition cycles, which is owing to lack of air convection. With more and more layers deposited, the peak temperature became lower because the sample became far from the heat source. It is worth mentioning that the formation of different kinds of α is involved in the cooling process, as shown in Fig. 4 [16]. So, the instantaneous cooling rate around β transus (950 ℃ in this study) is vital and calculated to be AD: 85.1 ℃/s, 1st TC: 46.3 ℃/s. The fasted cooling rates of the 2nd and 3rd TC are 19.7 ℃/s and 10.5 ℃/s, respectively.

3.2. Microstructure characterization

3.2.1. Prior β grains

The prior β grains formed during the solidification process of deposition and occurred variation during the subsequent thermal cycles. The corresponding β grains at different stages during the whole thermal cycle are shown in Fig. 5. From the overall view of the GBs distribution, the shape of β grains did not change significantly. However, it is apparent that some GBs still experienced certain degrees of migration, which can be proved especially from the marked area and the GBs. The marked area and GBs moved to different distances after separate thermal cycles, mainly related to two factors: i) Re-heating temperature. Higher temperature is more conducive to contributing to the migration energy of GB atoms, thereby increasing the moving distance of GBs. In this case, minor residual β nuclei will grow directly at high temperature, followed by meeting and merging with the previous β grains to form a new grain with different GB outlines; ii) Degree of α→β transformation. For each thermal cycle, different amounts of α phases transformed into β during the heating process, while some β phases kept not transformed to α and became retained β during the cooling process. As mentioned earlier, α phases nearing the GBs are more likely to transform at first. So, these α phases can form β phases and then prioritize contributing to the expansion of original β grains with the same orientation. The schematics of these two cases are shown in Fig. 6 respectively. Since the peak temperature and the degree of α→β transformation of the 1st TC are significantly higher than those of

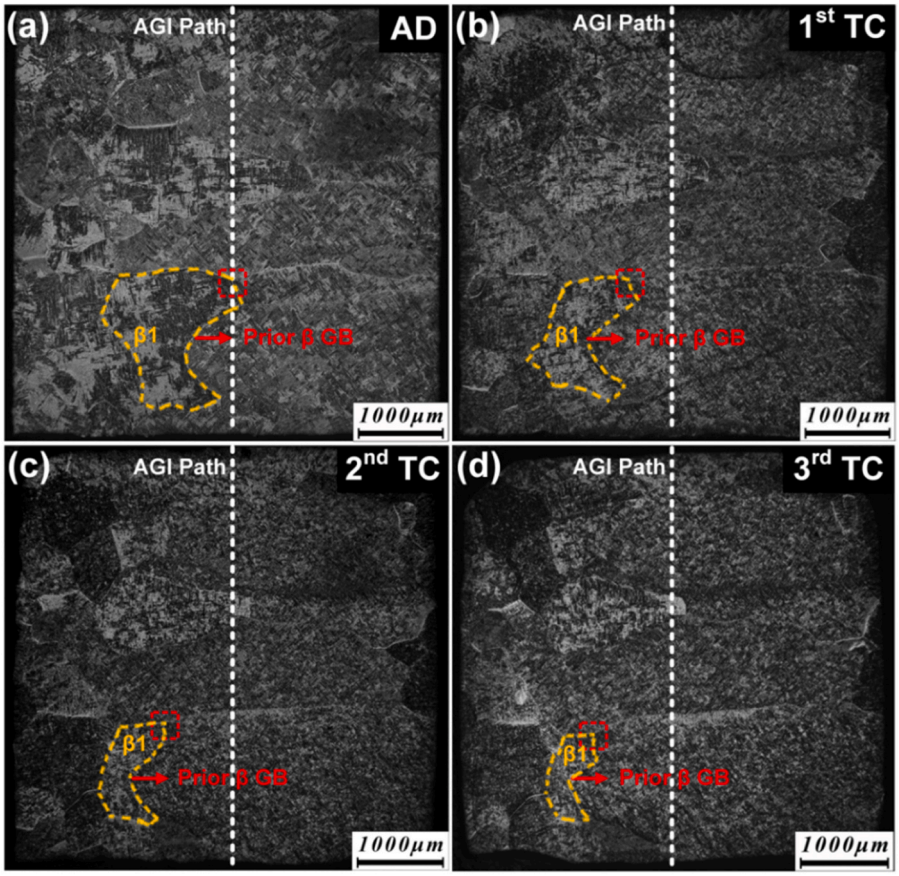

Fig. 5. Prior β grains at different states: (a) AD, (b) 1st TC, (c) 2nd TC, (d) 3rd TC.

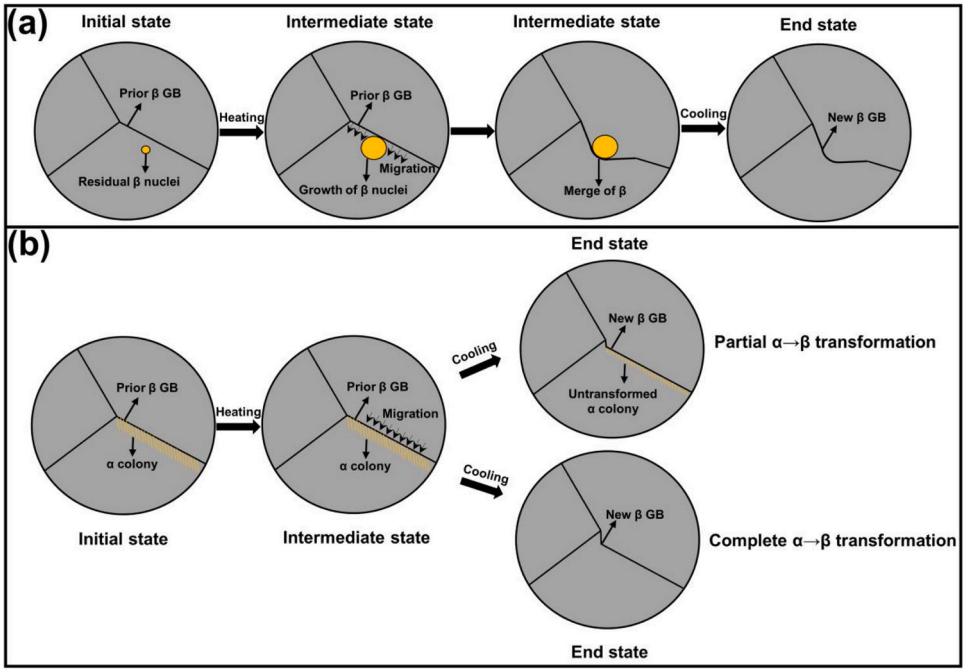

Fig. 6. Schematic of prior β GBs migration: (a) case (i) - GBs movement caused by high re-heating temperature, (b) case (ii) - newly formed GBs outline due to α→β transformation.

the other two thermal cycles, the GBs migration distance is the largest among them. In addition, the grain size of the sample after each thermal cycle was measured to be ~1.57/mm using the Average Grain Intercept (AGI) method (paths in Fig. 5), and the average area of each β grain after each thermal cycle is calculated to be ~1.6 mm^2 using ImageJ software, indicating that there is no significant change in the average size of prior β grains. However, due to the subsequent observation of α phases at higher magnifications in the marked areas, the effect of parent β grains size on the derived α phases must be considered [18,19]. Therefore, the area variation of specific β grains (β1) was measured after each thermal cycle with Image J software. From the grain outlines drawn in Fig. 5, the area of β1 grain showed a gradually decreasing trend, resulting in AD: 1.68 mm^2, 1st TC: 1.04 mm^2, 2nd TC: 0.54 mm^2, 3rd TC: 0.37 mm^2. This means that the size of the α_m colony inside the β grains also shows a decreasing trend [20].

3.2.2. Massive α (α_m)

This study mainly involves two types of α phases, including α_m and GB α. GB α normally nucleates at grain boundaries (GBs), grows, and distributes along GBs. α_m refers to the α lath that nucleates at GBs or GB α and then grows into the grain to form α colonies. Since GB α is too small and in close contact with α_m, which is hard to be distinguished in low magnification, SEM graphs are mainly used to deduce the evolution history of α_m. Fig. 7 shows the high-magnification SEM morphology of the red rectangular area in Fig. 5 after each thermal cycle. Fig. 7(a)-(d) shows the cross GBs of the three prior β grains for each state, which is used to precisely target the P1 position at high magnification. From the overall view of these graphs, no apparent features of the α/α' martensite phase are present, such as the morphology of blocky colonies formed with fine acicular α laths [21]. Fig. 7(e)-(h) represents the high-resolution graphs of the P1 position. It can be seen that α_m colonies with different distribution orientations formed at different GBs after deposition. To demonstrate the orientation change of α_m after different thermal cycles, IPF maps and the corresponding high magnification pole projection for the targeted area (α_{m1}) at the GB1 location were compared in Fig. 8.

The 1st TC is the complete transformation of α→β because the peak temperature (1249 ℃) is far higher than β transus. As mentioned above, GB migration results in the shrinkage of β1 grains. This implies the transition of the β orientation in the vicinity of the β1 GB to the orientation of the expanded β grains (upper grains). This caused the generated α to be different from the previous one during cooling and was also the reason for the reduction of the α_{m1} colony. Once again, due to the complete transformation of α, although the morphology of the remaining α_{m1} colony looks similar to the previous state (Fig. 7(e)) from the SEM graphs, it was found that the orientation of α_{m1} has been changed. When compared to the orientation with [−2 8 −6 −1] parallel to the macroscopic X_0 in Fig. 8(a), a similar orientation with [−3 10 −7 −1] that has a misorientation angle of 3.4° is generated after the high-temperature thermal cycle (1st TC) as shown by the circle in Fig. 8(b). Besides, new orientations such as [−4 9 −5 −18], [−8 17 −9 −22], and so on parallel to the X_0 appear in Fig. 8(b) as well, indicating the orientation diversity of the latest formed α_m laths. The shrinkage of β1 grains also makes it easier for α_m generated on different GBs to collide, meaning that α_{m1} has suffered growth inhibition from the α_{m3} originated at other GBs such as GB3. Due to the lower cooling rate and relatively long residence time of the microstructure at the high temperature during the 1st TC, α laths were significantly broadened, increasing from ~1 μm (AD) to ~1.5 μm (1st TC) on average width.

The microstructure after the 2nd TC is similar to that of the 1st TC because only partial α transformed to β. It can be deduced from some regions (white circles in Fig. 7) that the α→β→α transformation has occurred due to the significantly different α arrangement when compared to the first state. Apart from the white circle regions, some α→β transformations in other regions indeed lead to a decrease in the spacing between α laths, the disappearance of some secondary α laths (orange dashed circle), and the coverage of the α_{m1} region. However, for the regular and densely distributed α_{m1} colony, the SEM looks similar to the previous state (1st TC). The dominant orientation with [−2 6 −4 −1] parallel to the X_0 in Fig. 8(c) has a slight misorientation angle of 4.5° with the orientation of [−3 10 −7 −1] in Fig. 8(b). Therefore, it can be preliminary deduced that the entire α_{m1} laths near GB1 experienced α→β transformation during the 2nd TC due to the disappearance of orientation diversity and no orientation

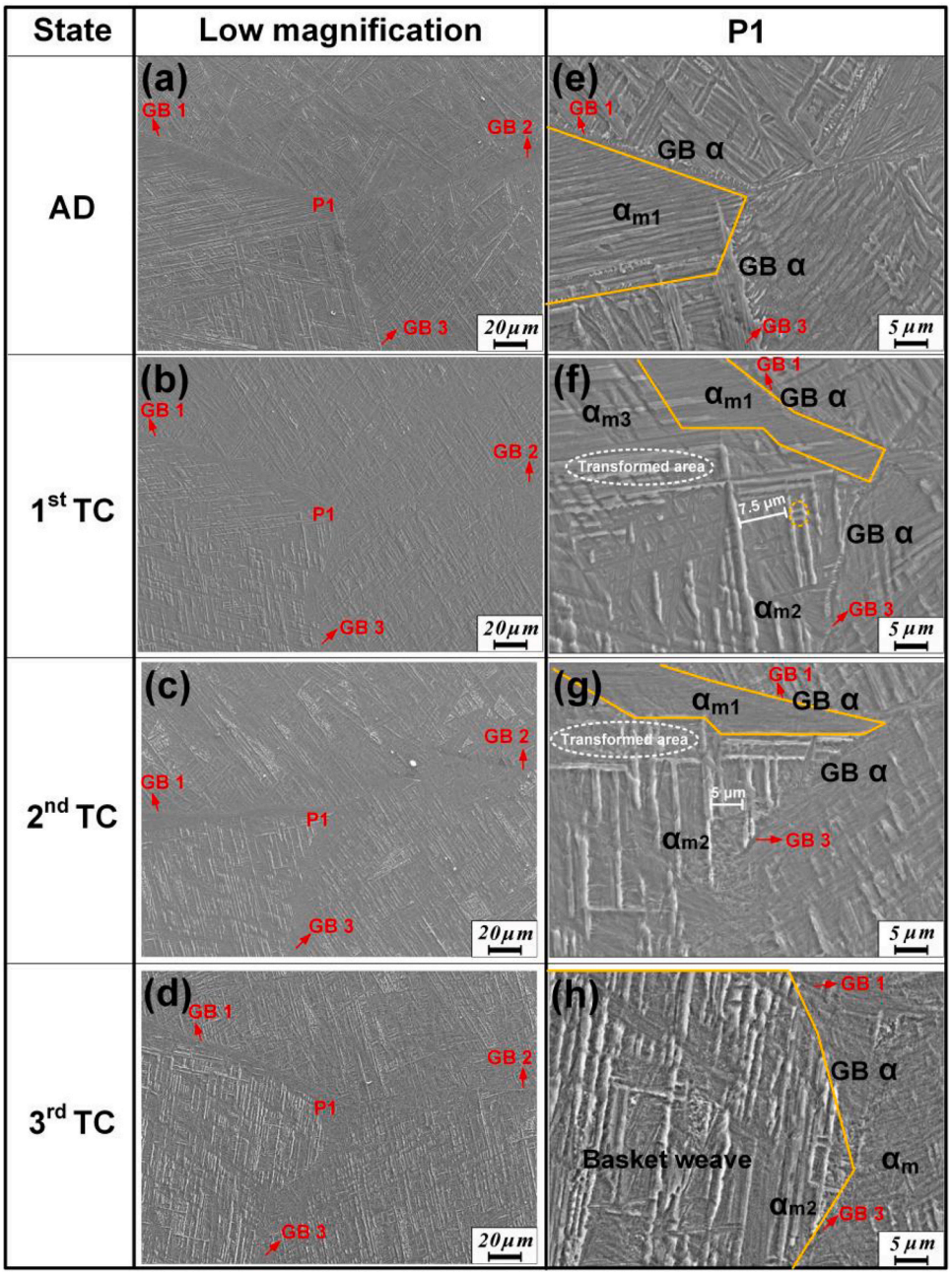

Fig. 7. SEM graphs of α_m grains at different states: (a), (e) AD, (b), (f) 1st TC, (c), (g) 2nd TC, (d), (h) 3rd TC.

same as previous ones. However, the slight misorientation angle difference between [−3 10 −7 −1] and [−2 6 −4 −1] parallel to the X_0 means that these newly formed α_{m1} laths still have a similar orientation as the one before experiencing the 2nd thermal cycle. Additionally, the average thickness of α laths in this region was reduced to ~1.2 μm compared with that of 1st TC.

Compared with the microstructure of the 2nd TC, the αm laths nearing GB become more dense and continuous after the 3rd TC. Since the peak temperature of this thermal cycle (630 ℃) is much lower than the β transus (950 ℃), only a small amount of α has undergone α→β transformation, and most of the untransformed α phases mainly experience grain growth process. This can be revealed from the comparison of Fig. 8(c), (d), referring that the α orientation of the entire region is almost unchanged. Opposing growth and meeting of dispersed short α laths results in many long and continuous α laths, shown in Fig. 7(g), (h). In addition, the previous remaining α_m located around the GB1 disappeared in the scope, representing the reduction of α_{m1}. Therefore, the bottom part of the α_{m1} region was sure to have transformed during the 3rd TC. This is because this part of the α_{m1} colony is the region in contact with α phases equipping other orientations, which has lattice distortion, further resulting in higher unstable energy and easy for α→β transformation. When cooling again, two conditions may exist: a) After β transformation, the α growing from other regions (such as the α_{m2} of GB3 below) occupies this area so that new α lath cannot form again. b) New α were generated during the cooling process. Moreover, these α laths have the same orientation as α_{m2}, further leading to the merge of α grains after growing. For the remaining part of α_{m1}, it can be deduced that there was no occurrence of α→β transformation, which can be proved from the same pole direction as the second state is shown in Fig. 8(d). As the cooling progresses, these α phases interlace with the α phases from other regions to form the fine

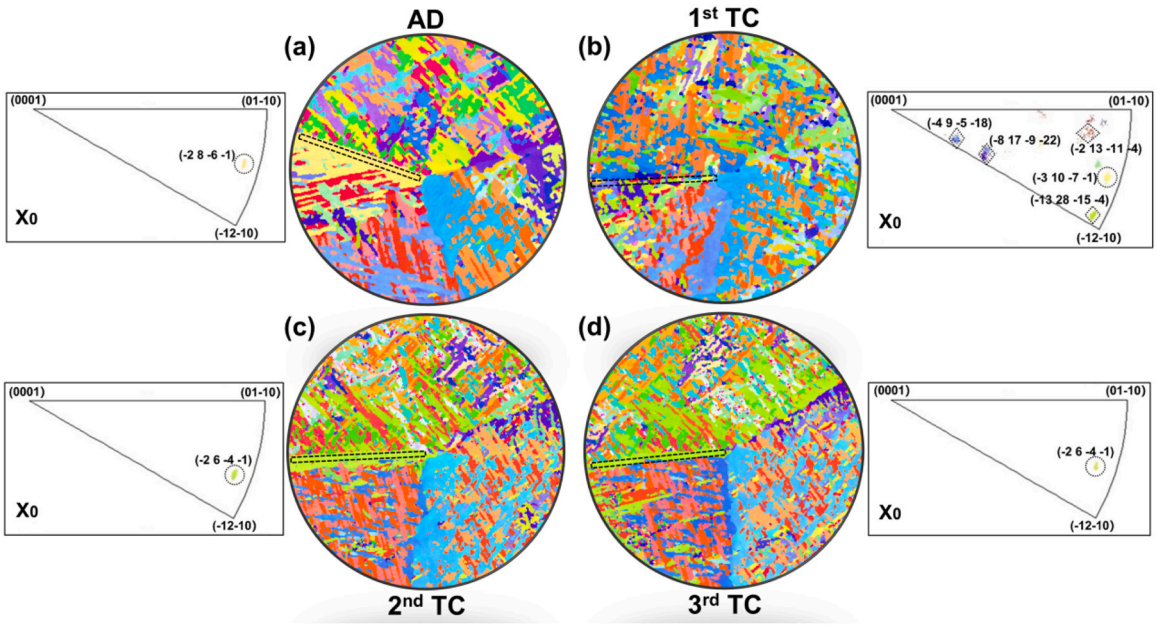

Fig. 8. IPF in Z_0 direction of the sample surface at different states: (a) AD, (b) 1st TC, 2nd TC, 3rd TC. (Pole points of the dashed line area at the different states, indices calculated by CaRIne Crystallography 3.1).

basketweave structure. The width of single α lath almost remains constant (1.1–1.2 μm) owing to low heating temperature and short dwell time at relatively high temperatures (> 500 ℃).

Overall, after the three thermal cycles, α_m generated at the GB1 was gradually occupied by α laths originating from other regions. This was caused by the expansion of adjacent prior β grains and contributed by the competitive growth [22] of other GB α_m inside the same β grains. The average size of α_m phases was significantly broadened and occurred orientation diversification after experiencing a high-temperature thermal cycle (1st TC). When undergoing partial α→β transformation, since the peak temperature of the 2nd TC was still high, the proportion of transformed α was relatively large. This means that the newly formed α laths account for a major part, resulting in a decreased α width. Besides, the entire αm near the GB1 took place α→β transformation, while newly formed α laths remain in a consistent orientation and similar to one of the orientations that existed before. However, for the low-temperature thermal cycle (3rd TC), partially retained α_m colony at and nearing GB1 did not undergo α→β transformation but some α_m located at the orientation transition border transformed. This shows that the decrease in thermal cycle temperature can no longer contribute to the instability of the GB to induce phase transformation. However, the lattice distortion energy between different orientations can still provide sufficient energy. This transformed α became the same

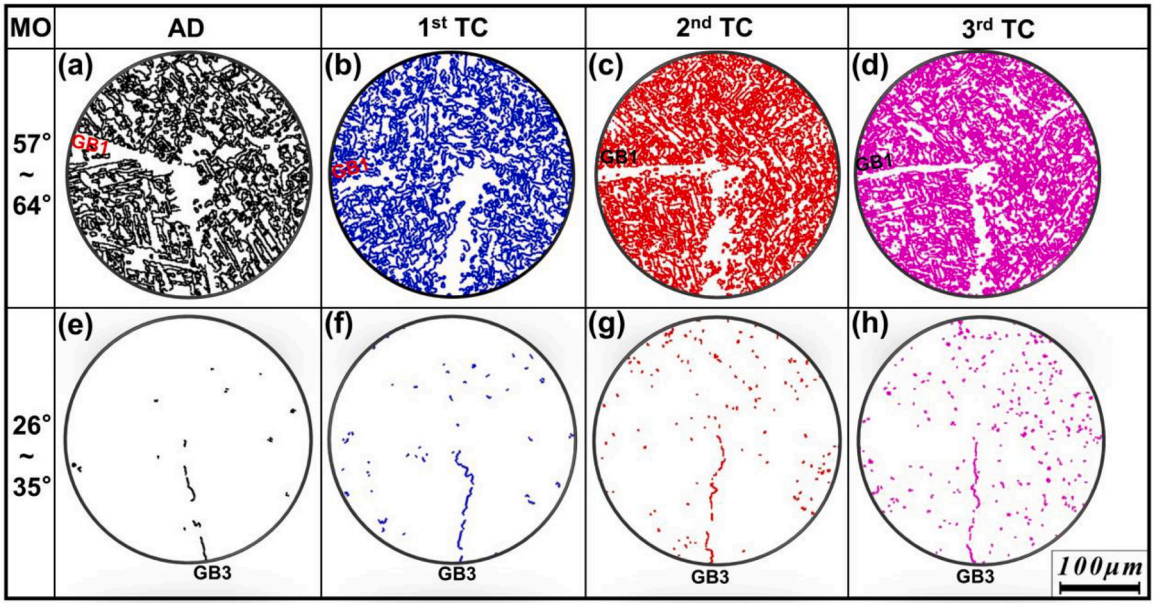

Fig. 9. Misorientation of α grains near the GBs at different states: (a), (e) AD, (b), (f) 1st TC, (c), (g) 2nd TC, (d), (h) 3rd TC.

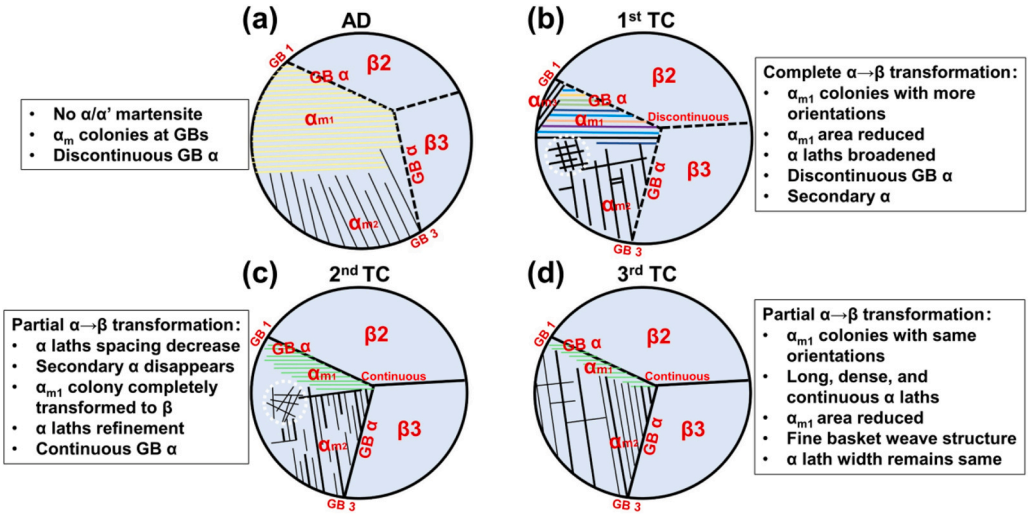

Fig. 10. The overall α phases evolution of the entire thermal cycle: (a) AD, (b) 1st TC, (c) 2nd TC, (d) 3rd TC.

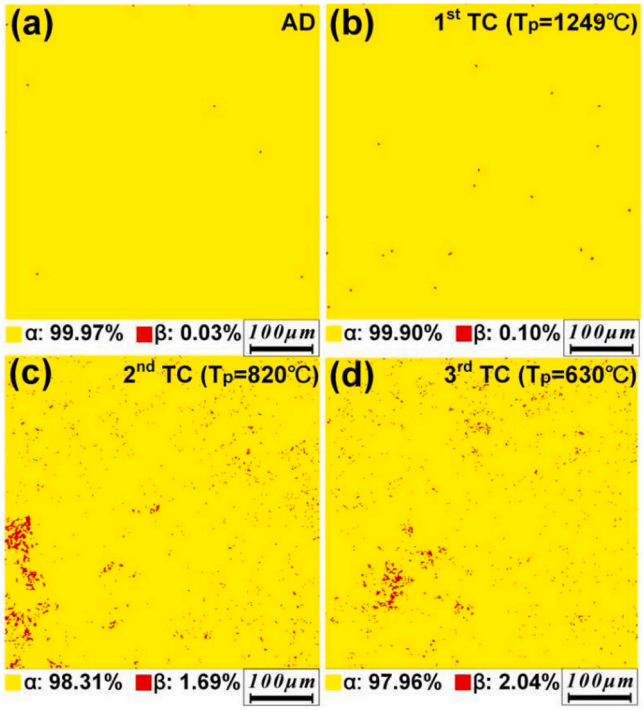

Fig. 11. Phase map of different states.

Table 3
Phase transformation of the entire thermal cycle.

Processes	Phases at the start state	Transformation	Phases at the end state
AD	Liquid	Liquid → β → α_m Liquid → β → GB α	α_m Retained β
1st TC	α_m GB α	Complete α_m → β → α_m Complete GB α → β → GB α	GB α Basket weave
2nd TC	α_m GB α	Complete (Later): α_m → β	
3rd TC	α_m Retained β GB α	Complete/partial GB α → β β → GB α β → α_m	

orientation as the surrounding α, which is far from GB1, causing a significant increase in length, even though the average width remains unchanged.

3.2.3. Grain boundary α (GB α)

Fig. 9 shows the Misorientation (MO) of α phases in different states near the GB1 and GB3. Firstly, the blank areas near GB1 and GB3 refer to the previous α_m colony, which intuitively shows a decreasing trend with the progress of thermal cycles. This effectively verifies the previous conclusion obtained in the 3.3.2 section. The misorientation of the majority of α laths is between 57° and 64°, which is consistent with the conclusions obtained by previous studies [23,24]. It is worth pointing out that the GB α growing on the GB3 shows misorientation between 26° and 35°, which does not belong to the range of the five α orientation relationship [23]. This is because angle ranges were determined based on the α phases coming from different β grains instead of the same parent β.

Additionally, the degree of continuity of GB α has an essential impact on mechanical properties such as microhardness and tensile strength [25]. It can be found that the continuity of GB α in both AD and 1st TC states is significantly worse than that of 2nd TC and 3rd TC. This is because the GB α of the first two states formed at relatively low temperatures (~600 ℃), in which case that there are already many α_m generated from GBs, GB α can only form by the interspersed way between α laths. The difference is that GB α is prioritized for the last two thermal cycles, which can preferentially grow along the GBs to achieve a continuous structure. So far, the overall α phase evolution of the entire thermal cycle is summarized in Fig. 10. With this to point out that the α_{m1} laths in Fig. 10(a), Fig. 10(b)-orange, and Fig. 10(c),(d) are considered to have similar orientations due to their insignificant misorientation angles are 3.4° as mentioned above and 4.5°respectively.

3.2.4. Summary of phase evolution

Based on the typical cooling rates calculated above (Section 3.1) and combined with the peak temperatures of thermal cycles, the critical cooling rate for phase formation shown in Fig. 4, as well as the microstructural characterization (Section 3.2), the phase evolution throughout the whole thermal cycles can be reproduced. Firstly, the 1st TC is related to the complete transformation of α, while the 2nd TC and 3rd TC refer to the partial α→β transformation because of the peak temperatures lower than β transus. It can be judged that there is no α/α' martensitic formation for the entire thermal cycle

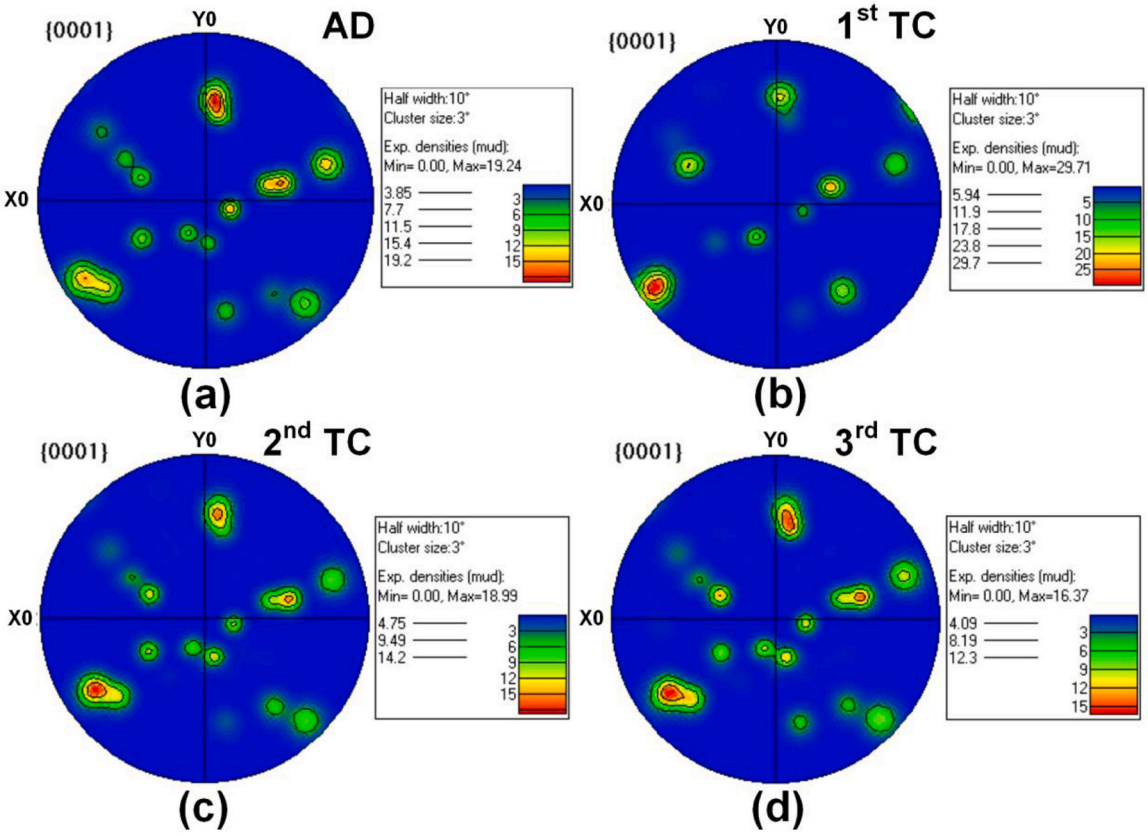

Fig. 12. Pole figure of the sample at different states: (a) AD, (b) 1st TC, (b) 2nd TC, (3) 3rd TC.

because the cooling rate is far smaller than 410 ℃/s. The instantaneous and average cooling rates (> 500 ℃) of AD and 1st TC are much larger than 20 ℃/s near and even far beneath the β transus. This means that most α phases directly nucleated based on the grain boundaries (GB) and grew to be massive α (α_m). As the cooling rate kept decreasing with cooling progress, the GB α (shell [22]) started to form when the cooling rate was just below 20 ℃/s (around 600 ℃ for deposition and 1st TC). Because the peak temperature of the 2nd TC is high, most of α_m still took place α→β transformation. Moreover, due to the high energy and more defects accumulated at the GB, α phases surrounding GBs are more unstable and easy to transform, which can be revealed by the abovementioned EBSD. Besides, owing to the fastest cooling rate, just below 20 ℃/s near the peak temperature for the 2nd TC, the GB α layer formed first, which is different from the deposition and 1st TC processes. With the progress of cooling, long parallel α_m started to form at the root of the GB α layer. Compared with the 2nd TC, on the one hand, the instantaneous and average cooling rates of the 3rd TC and the peak temperature were significantly reduced. On the other hand, T. Ahmed [17] reported that the initial formation temperature of α_m will be higher than β transus with the cooling rate decreases. This means that the stability of α_m was improved as well. Therefore, most α_m has an unfavorable potential to proceed with α→β transformation. For each thermal cycle, with the temperature cooled down and the cooling rate decreased further and further, α_m also grew into the grain center and formed the basket weave structure. In addition, multiple thermal cycles and slow cooling rates also promote elemental diffusion effects, causing regional segregation of β stabilizer elements, leading to more retained β, as shown in Fig. 11. In general, the phase transformation of the entire thermal cycle is summarized in Table 3.

3.2.5. Anisotropy

In this study, the {0001} lattice plane family was used as a reference to show the anisotropy of the samples. Theoretically, if various α variants are formed and distributed uniformly, then the intensity distribution of the {0001} planes should be uniform also, and the intensity ratio of the poles should be 1. If the strongest-to-weakest pole ratio is greater than 1, there are cases of α variant selection. This selection tendency became more severe as the ratio increased. Although using the characterization results of such a small sample to represent the entire printed wall was highly possible to have some deviations, there is still necessary to proceed and show a general changing trend. Thus, the pole figure shown in Fig. 12 calculated that the maximum/minimum pole intensity ratio was 4.99, 5, 2.99, and 3.00.

Furthermore, the maximum multiples of uniform distribution (MUD) values of α phases at AD and 1st TC states are significantly larger than 2nd TC and 3rd TC. This indicates that the deposition process and high-temperature thermal cycling of complete β transformation resulted in a strong preferred orientation for α variants. After the high-temperature partial transformation (1st TC), most of the α variants reformed with different orientations. This can be attributed to the cooling rate significantly reducing the preferred orientation [26]. However, during the low-temperature partial transformation (2nd TC), most α laths did not transform. Even the

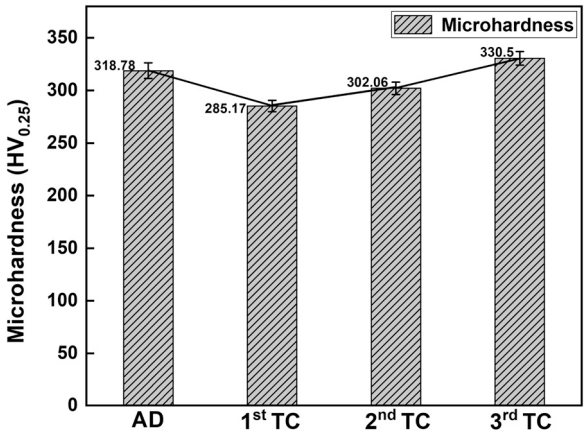

Fig. 13. Microhardness in different states.

transformed α will follow the nearby α orientation, so the preferred orientation was almost unchanged.

3.3. Microhardness

The microhardness of the samples after each thermal cycle was measured. Multiple points were randomly taken on the targeted region periphery of the sample (surrounding the β1 grains), and the average value was taken as the microhardness of the whole sample. The final result is shown in Fig. 13. It can be found that the microhardness after the 1st TC significantly decreased from 318.78 ± 7.5 HV to 285.17 ± 5.3 HV. As mentioned in IPF (Figs. 8(a) and 8(b)), a significant change of 1st TC is the orientation diversity of massive α formed at GB, which is favorable for the area reduction of α colony and increases the microhardness [27]. However, the constant maximum/minimum pole intensity ratio (5 and 4.9 in Figs. 12(a) and 12(b)) indicated that such local orientation diversity did not play a role for the entire sample after the 1st TC, which seems owing to more formation of α colony with a same orientation at other locations (inner grain). In this case, the broadening effect of α laths (grain coarsening effect) became the main factor contributing to the microhardness instead of the area reduction of α colony caused by local orientation diversity.

After the 2nd TC, the orientation diversity of massive α formed at GB was eliminated as shown in Figs. 8(b) and 8(c), so that α lath colonies with the preferred orientation (−2 6 −4 −1) formed at GB. Besides, there are also many α lath colonies with different orientations formed inside grains (Fig. 8(c)). Such α colonies normally contribute to the decrease of microhardness but the degree is depended on the size of the colony. Besides, based on the previous report about GB α, continuous GB α results in severe dislocations pile-up around the prior β GBs, which induces significant stress concentration and increases the density of nucleation sites of the micro-voids. Then the micro-void coalescence leads to the crack. This is why the higher microhardness and yield strength of continuous GB α [28]. Therefore, after 2nd TC, GB α transforms from a discontinuous to a continuous state (Fig. 9) as well as a reduced average width of α laths, improved microhardness to 302.06 ± 5.9 HV. It can be known that the formation of α colonies (< 5 μm) with the same orientation inside the grains has a limited effect on microhardness.

After the 3rd TC, α laths inside the grain became longer and more continuous, thus hindering the propagation of cracks more effectively. In addition, the area of the α_m colony with the orientation (−2 6 −4 −1) decreased from ~2368 μm^2 to ~978 μm^2 which was revealed by Figs. 8(c) and 8(d), further increasing microhardness. Thus, thermal cycles created a gradient variation of the microhardness and possible tensile strength between layers. This is mainly reflected in the middle section, which refers to the stable deposition with the same effective thermal cycles. The top section refers to fewer and fewer thermal cycles with layer increases of the components. The position with the worst performance occurs in the top penultimate deposited layer that has merely experienced once complete β transformation rather than other top layers. The rest regions of the sample are considered to be the stable deposition zone that experienced three effective thermal cycles, showing the highest microhardness of 330.5 ± 6.4 HV.

3.4. Corrosion resistance

Electrochemical corrosion resistance is an essential characteristic of titanium alloys fabricated by the wire-arc DED process. Many variants can be used to characterize this performance, such as corrosion potential (E_{corr}), which evaluates the activation difficulty of corrosion reaction at the initial state, corrosion current density (i_{corr}) which reflects the velocity of corrosion reaction rate and the current of passive state (i_{pass}) which mainly decides the difficulty of oxidation reaction at the stable state and the resistance of the sample [29,30]. Therefore, this study mainly investigated the changes of these four variables in the initial (AD) state and the final state (after the entire thermal cycle), which are revealed in Fig. 14. Based on the Electrochemical polarization Tafel curves shown in Fig. 14(a) and the corrosion parameters listed in Table 4, we can see that the E_{corr}, i_{corr}, and i_{pass} significantly increased when the sample experienced the entire thermal cycle. This means that the corrosion resistance became deteriorated. The corrosion activation in the initial state becomes more straightforward, and the corrosion rate at the stable (passive) state becomes faster, which leads to a shorter corrosion life [12]. During the corrosion process, the formation of an oxidation passive film can be observed, which was revealed by the temporarily decreased current on Tafel curves (some fluctuations). The formed passive film on the surface including a thin oxide layer or passivization compound would protect the inner alloy and temporarily prevent the corrosion process to a certain degree. However, with the corrosion potential increasing, the passive film will be broken, causing further corrosion of the internal alloy and the corrosion rate rising again. After a few more cycles, the sample corrosion reached a passive state and performed a stable corrosion rate. For the sample that experienced the entire thermal cycle, the more significant current variation caused by oxide film formation and breaking is attributed to the larger thickness of oxide film due to worse corrosion resistance (higher corrosion current peak). The thicker oxide film, in turn, brought a better protection effect to internal alloys (lower corrosion current valley). In addition, the general electrochemical impedance method, Electrochemical impedance spectra (EIS), was performed. The simulation results were obtained from the designed equivalent circuit (Fig. 14(d)) using ZView 4 software, and the experimental results have acquired good fitting. It adopted the Nyquist and Bode plot to evaluate the polarization resistance (R_p) [31]. The larger arc radius of the curve in the Nyquist plot represents a greater R_p, and the ability of corrosion resistance is better [32].

As a result, a decrease of R_p from 14.23 kΩ·cm^2 to 7.80 kΩ·cm^2 is considered to be the indispensable factor for the weakened corrosion resistance of the sample. As mentioned above, the change in the microstructure is a possible reason for further R_p variation and corrosion resistance degeneration. First, the broadening of α lath after the entire thermal cycle is one of the main reasons for the decrease in corrosion resistance [33]. Besides, even though some studies have pointed out that the increase of β phase content helps to improve corrosion resistance [34], the influence of increased β phase content in this study is insignificant. Conversely, the increased β phase makes alloying element segregation more severe, resulting in the significant galvanic effect between α and β phases to

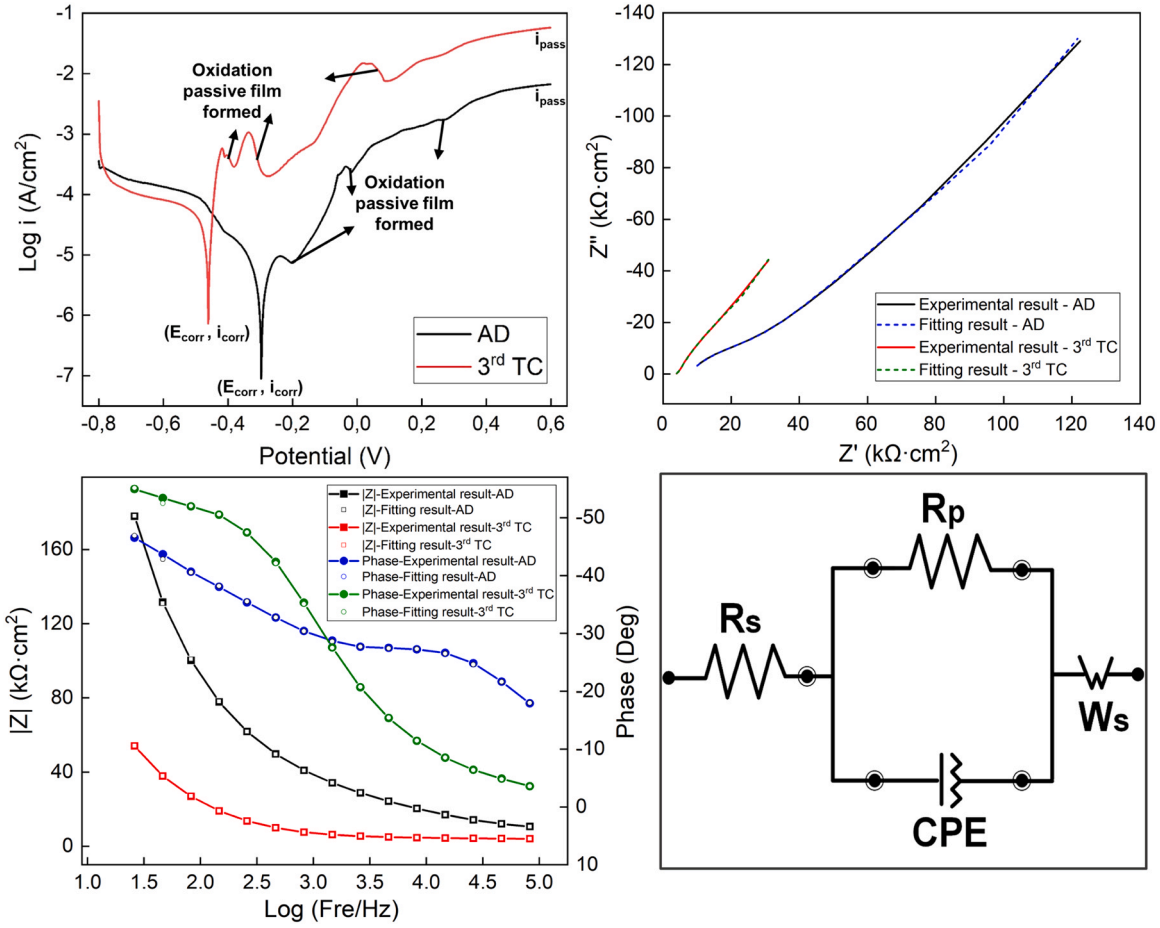

Fig. 14. Results of Electrochemical corrosion test: (a) Electrochemical polarization Tafel curves, (b) EIS - Nyquist plots, (c) EIS - Bode plots, (d) EIS - equivalent circuit.

Table 4
Corrosion parameters of the Ti-6Al-4 V sample manufactured by wire-arc DED process.

States	E_{corr} (V)	i_{corr} (A/cm^2)	i_{pass} (A/cm^2)	R_p (kΩ·cm^2)
AD	-0.30	0.86×10^{-7}	6.57×10^{-3}	14.23
3rd TC	-0.46	0.73×10^{-6}	5.75×10^{-2}	7.80

accelerate the corrosion process. Therefore, the analysis of the above results shows that the Ti-6Al-4 V components fabricated by wire-arc DED process have non-uniformity in corrosion resistance along the deposition direction. Multiple thermal cycles decrease corrosion resistance, resulting in the performance difference between the sample top (thermal cycle gradient) and bottom regions (same thermal cycles).

4. Conclusions

This study investigated the effect of multiple thermal cycles on Ti-6Al-4 V deposits fabricated by wire-arc DED process with the help of Gleeble TMS, a numerical simulation model, and Ti-6Al-4 V single-bead wall deposition. The main conclusions are summarized as follows:

(1) With the assistance of the Gleeble TMS test, the thermal cycles that occur during the wire-arc DED process were successfully simulated. The good feasibility of using Gleeble TMS to efficiently and intuitively explore the thermal cycle effect was shown in this work.

(2) Some prior β GBs migrate significantly during the high-temperature thermal cycle (1st TC-1249 °C), but the overall average β grain shape and size remain unchanged. The content of retained β increased with the thermal cycles.

(3) α_m colony nearing GBs was occupied, and partially disappeared owing to a comprehensive effect of competitive growth, complete/incomplete α→β transformations, and β GBs migration. The broadening effect happened on α_m laths after the entire thermal cycle. Due to lower formation temperature, the GB α became more continuous with the thermal cycles progressing.

(4) Thermal cycles at low- and medium- temperatures (partial α→β transformation) ease the microstructure anisotropy produced by deposition and high-temperature (complete α→β transformation) thermal cycle.

(5) After the entire thermal cycle, the microhardness increased from 318.78 ± 7.5 HV to 330.5 ± 6.4 HV. However, the microhardness after the high-temperature thermal cycle dropped sharply to 285.17 ± 5.3 HV, mainly due to the grain coarsening.

(6) The corrosion resistance of the samples decreased after the entire thermal cycle, indicating a performance difference between the top (thermal cycle gradient) and bottom regions (same thermal cycles).

CRediT authorship contribution statement

Zidong Lin: Methodology, Conceptualization, Writing - original draft. **Lixue Qiao:** Samples printing and characterization, writing - review & editing. **Zhen Sun & Yongzhe Fa:** Data analysis, writing - review & editing. **Rui Cao, Wei Ya, Yan Li, Constantinos Goulas &**

Xinghua Yu: Supervision, Conceptualization, Writing - review & editing.

Data availability

No data was used for the research described in the article.

Declaration of Competing Interest

The authors declare that they have no known competing financial interests or personal relationships that could have appeared to influence the work reported in this paper.

Acknowledgments

The work is sponsored by National Key Laboratory Foundation of Science and Technology on Materials under Shock and Impact 2021ZX52002222019 and the Beijing Institute of Technology Young Scholar Startup Program. The authors gratefully acknowledge financial support from China Scholarship Council (CSC No: 202106030118) and technical support from the Experimental Center of Advanced Materials (ECAM) of the Beijing Institute of Technology.

References

[1] W. Ya, C. Goulas, K. Hamilton, M. Hermans, G.-W. Römer, I. Richardson, Microstructure and mechanical properties of CuAl8Ni6 produced by Wire Arc Additive Manufacturing for marine applications, European Congress and Exhibition on Advanced Materials and Processes, EUROMAT, (2017).
[2] Z. Lin, K. Song, W. Ya, X. Yu, Parametric and metallurgical investigation of modified 3D AM 80 HD steel for wire and arc additive manufacturing, Journal of Physics: Conference Series, IOP Publishing, 2021012049.
[3] Z. Lin, Wire and Arc Additive Manufacturing of Thin Structures Using Metal-Cored Wire Consumables: Microstructure, mechanical properties, and experiment-based thermal model, (2019).
[4] Z. Lin, P. Liu, X. Yu, A literature review on the wire and arc additive manufacturing—welding systems and software, Sci. Adv. Mater. 13 (8) (2021) 1391–1400.
[5] G. Welsch, R. Boyer, E. Collings, Materials properties handbook: titanium alloys, ASM Int. (1993).
[6] J. Alcisto, A. Enriquez, H. Garcia, S. Hinkson, T. Steelman, E. Silverman, P. Valdovino, H. Gigerenzer, J. Foyos, J. Ogren, Tensile properties and microstructures of laser-formed Ti-6Al-4V, J. Mater. Eng. Perform. 20 (2011) 203–212.
[7] Jia Yang, Wanqi Zhao, Panpan Lin, Qiuguang Zhang, Xinfei Zhang, Tiesong Lin, Peng He, Yanli Zhuang, An efficient method to engage oxide ceramics in low-temperature interfacial reactions: microstructure evolution and kinetics behaviors based on supercooling in a transient liquid phase bonding joint, J. Mater. Sci. Technol. (2023), https://doi.org/10.1016/j.jmst.2022.10.094
[8] Y. Zhou, G. Qin, L. Li, X. Lu, R. Jing, X. Xing, Q. Yang, Formability, microstructure and mechanical properties of Ti-6Al-4V deposited by wire and arc additive manufacturing with different deposition paths, Mater. Sci. Eng.: A 772 (2020) 138654.
[9] G. Xian, J. Lee, S.M. Cho, J.-T. Yeom, Y. Choi, N. Kang, Effect of heat input on microstructure and mechanical property of wire-arc additive manufactured Ti-6Al-4V alloy, Weld. World 66 (5) (2022) 847–861.
[10] J. Kennedy, A. Davis, A. Caballero, M. White, J. Fellowes, E. Pickering, P. Prangnell, Microstructure transition gradients in titanium dissimilar alloy (Ti-5Al-5V–5Mo-3Cr/Ti-6Al-4V) tailored wire-arc additively manufactured components, Mater. Charact. 182 (2021) 111577.
[11] S. Wang, M. Aindow, M. Starink, Effect of self-accommodation on α/α boundary populations in pure titanium, Acta Mater. 51 (9) (2003) 2485–2503.
[12] L. Chen, J. Huang, C. Lin, C. Pan, S. Chen, T. Yang, D. Lin, H. Lin, J. Jang, Anisotropic response of Ti-6Al-4V alloy fabricated by 3D printing selective laser melting, Mater. Sci. Eng.: A 682 (2017) 389–395.
[13] B. Wu, Z. Pan, S. Li, D. Cuiuri, D. Ding, H. Li, The anisotropic corrosion behaviour of wire arc additive manufactured Ti-6Al-4V alloy in 3.5% NaCl solution, Corros. Sci. 137 (2018) 176–183.
[14] Z. Sun, X. Yu, Prediction of welding residual stress and distortion in multi-layer butt-welded 22SiMn2TiB steel with LTT filling metal, J. Mater. Res. Technol. 18 (2022) 3564–3580.
[15] Z. Lin, K. Song, B. Di Castri, W. Ya, X. Yu, Microstructure-gradient approach for effective determination of post-heat treatment temperature of an additive manufactured Ti-6Al-4V sample, J. Alloy. Compd. 921 (2022) 165630.
[16] S. Liu, Y.C. Shin, Additive manufacturing of Ti6Al4V alloy: a review, Mater. Des. 164 (2019) 107552.
[17] T. Ahmed, H. Rack, Phase transformations during cooling in α+ β titanium alloys, Mater. Sci. Eng. A 243 (1–2) (1998) 206–211.
[18] I. Sen, S. Tamirisakandala, D. Miracle, U. Ramamurty, Microstructural effects on the mechanical behavior of B-modified Ti–6Al–4V alloys, Acta Mater. 55 (15) (2007) 4983–4993.
[19] J. Tiley, T. Searles, E. Lee, S. Kar, R. Banerjee, J. Russ, H. Fraser, Quantification of microstructural features in α/β titanium alloys, Mater. Sci. Eng. A 372 (1–2) (2004) 191–198.
[20] G. Lütjering, Influence of processing on microstructure and mechanical properties of (α+ β) titanium alloys, Mater. Sci. Eng. A 243 (1–2) (1998) 32–45.
[21] X.-L. Gao, L.-J. Zhang, J. Liu, J.-X. Zhang, A comparative study of pulsed Nd: YAG laser welding and TIG welding of thin Ti6Al4V titanium alloy plate, Mater. Sci. Eng.: A 559 (2013) 14–21.
[22] A. Davis, J. Donoghue, J. Kennedy, N. Byres, P. Prangnell, In-situ observation of single variant α colony formation in Ti-6Al-4V, Acta Mater. 220 (2021) 117315.
[23] Q. Chao, P.D. Hodgson, H. Beladi, Ultrafine grain formation in a Ti-6Al-4V alloy by thermomechanical processing of a martensitic microstructure, Metall. Mater. Trans. A 45 (5) (2014) 2659–2671.
[24] J. Lin, Y. Lv, Y. Liu, Z. Sun, K. Wang, Z. Li, Y. Wu, B. Xu, Microstructural evolution and mechanical property of Ti-6Al-4V wall deposited by continuous plasma arc additive manufacturing without post heat treatment, J. Mech. Behav. Biomed. Mater. 69 (2017) 19–29.
[25] K. Cheng, M. Zhang, H. Song, X. Liu, Z. Fan, G. Wang, H. Zhang, Additive manufacturing of Ti-6Al-4V alloy by hybrid plasma-arc deposition and microrolling: grain morphology, microstructure, and tensile properties, Sci. China Technol. Sci. 65 (4) (2022) 849–857.
[26] G. Sargent, K. Kinsel, A. Pilchak, A. Salem, S. Semiatin, Variant selection during cooling after beta annealing of Ti-6Al-4V ingot material, Metall. Mater. Trans. A 43 (10) (2012) 3570–3585.
[27] N.K. Babu, S.G.S. Raman, R. Mythili, S. Saroja, Correlation of microstructure with mechanical properties of TIG weldments of Ti–6Al–4V made with and without current pulsing, Mater. Charact. 58 (7) (2007) 581–587.
[28] J. Wang, X. Lin, M. Wang, J. Li, C. Wang, W. Huang, Effects of subtransus heat treatments on microstructure features and mechanical properties of wire and arc additive manufactured Ti–6Al–4V alloy, Mater. Sci. Eng.: A 776 (2020) 139020.
[29] Y.M. Tan, R.W. Revie, Heterogeneous electrode processes and localized corrosion, John Wiley & Sons, 2012.
[30] B.R. Barnard, P.K. Liaw, R.A. Buchanan, O.N. Senkov, D.B. Miracle, Oxidation behavior of Ca-based bulk amorphous materials, Mater. Trans. 48 (7) (2007) 1870–1878.
[31] S.-M. Park, J.-S. Yoo, Peer reviewed: electrochemical impedance spectroscopy for better electrochemical measurements, ACS Publications, 2003.
[32] M.P. Pujadó, Carbon nanotubes as platforms for biosensors with electrochemical and electronic transduction, Springer Science & Business Media, 2012.
[33] J. Li, X. Lin, M. Zheng, J. Wang, P. Guo, T. Qin, M. Zhu, W. Huang, H. Yang, Distinction in anodic dissolution behavior on different planes of laser solid formed Ti-6Al-4V alloy, Electrochim. Acta 283 (2018) 1482–1489.
[34] N. Tomashov, G. Chernova, Y.S. Ruscol, G. Ayuyan, The passivation of alloys on titanium bases, Electrochim. Acta 19 (4) (1974) 159–172.